Band engineering in Mg_3Sb_2 by alloying with Mg_3Bi_2 for enhanced thermoelectric performance

Kazuki Imasato,[1] Stephen Dongmin Kang,[1,2] Saneyuki Ohno,[1,2†] G. Jeffrey Snyder[1‡]

[1]Department of Materials Science and Engineering, Northwestern University, Evanston, IL 60208, USA
[2]Department of Applied Physics and Materials Science, California Institute of Technology, Pasadena, CA 91125, USA

Abstract

Mg_3Sb_2-Mg_3Bi_2 alloys show excellent thermoelectric properties. The benefit of alloying has been attributed to the reduction in lattice thermal conductivity. However, Mg_3Bi_2-alloying may also be expected to significantly change the electronic structure. By comparatively modeling the transport properties of n- and p-type Mg_3Sb_2-Mg_3Bi_2 and also Mg_3Bi_2-alloyed and non-alloyed samples, we elucidate the origin of the highest *zT* composition where electronic properties account for about 50 % of the improvement. We find that Mg_3Bi_2 alloying increases the weighted mobility while reducing the band gap. The reduced band gap is found not to compromise the thermoelectric performance for a small amount of Mg_3Bi_2 because the peak *zT* in unalloyed Mg_3Sb_2 is at a temperature higher than the stable range for the material. By quantifying the electronic influence of Mg_3Bi_2 alloying, we model the optimum Mg_3Bi_2 content for thermoelectrics to be in the range of 20-30%, consistent with the most commonly reported composition $Mg_3Sb_{1.5}Bi_{0.5}$.

Introduction

Thermoelectric materials have the ability to convert heat directly into electricity without any mechanical motion.[1,2] Since the main obstacle for wide-use of thermoelectrics is the low conversion efficiency limited by the materials, material research has been focused on developing high efficiency materials.

The maximum power and efficiency achievable by a particular thermoelectric material is determined by their figure of merit $zT=(S^2\sigma)/\kappa T$ where *S* is the Seebeck coefficient, σ is the electrical conductivity, κ is the thermal conductivity and T is the absolute temperature. Strategies to enhance *zT* can be largely categorized into two different methods. One is by reducing the lattice thermal conductivity, for example, by increasing phonon scattering with alloying.[3–8] The other is by changing the electronic structure, *i.e.* band engineering.[9–13]

A recently developed new material where both strategies were successfully used to reach a high $zT\approx1.5$ is n-type $Mg_{3+x}Sb_2$ $Bi_{0.49}Te_{0.01}$, first reported by Tamaki et al[14] and followed by other groups.[15–17] Excess-Mg nominal compositions (x as high as 0.2) were used to synthesize n-type compounds and take advantage of the multi-valley conduction band as predicted by density functional theory (DFT) calculations (Fig.1).[14] The thermodynamic explanation behind this excess-Mg strategy to overcome the persistent p-type behavior[18–21] was later clarified by Ohno *et al*.[16] Mg_3Bi_2-alloying was introduced to reduce the lattice thermal conductivity, because Mg_3Sb_2 and Mg_3Bi_2 are expected to form solid solutions. Te-doping was used to optimize the carrier concentration.

In previous studies, the role of Bi in enhancing *zT* has mostly been attributed to Sb-Bi disorder that

† Present address: Institute of Physical Chemistry, Justus-Liebig-University Giessen, Heinrich-Buff-Ring 17, D-35392 Giessen, Germany

‡ Electronic mail: jeff.snyder@northwestern.edu

reduces thermal conductivity by disorder scattering of phonons.[14,15,17] However, alloying Mg_3Sb_2 with Mg_3Bi_2 also has a significant impact on the electronic structure.[14] This influence is readily anticipated by the fact that Mg_3Bi_2 is a semi-metal while Mg_3Sb_2 is a semiconductor.[18–20,22,23] Figure 1 illustrates the features of the electronic structure that is expected to change with the alloying of Mg_3Bi_2, based on DFT calculations. In addition to the reduction of the band gap, the band effective mass of individual bands (m_b^*) is also expected to decrease with Mg_3Bi_2 alloying. Such correlation between m_b^* and E_g is a commonly observed tendency explained with the interaction between the valence and conduction bands.[24] Furthermore, the shift of bands due to alloying, in general, could cause band convergence that is beneficial for thermoelectric properties.[12] These changes in the electronic structure suggest that there would be an optimum Mg_3Bi_2 content. More Mg_3Bi_2 would result in increased mobility due to the lighter m_b^*; however, a reduced band gap would compromise the peak *zT* value because of the onset of bipolar conduction being shifted to lower temperatures.[25,26] In addition to the competing changes in electronic properties, the lattice thermal conductivity of the compounds will have a minimum when the fraction of Bi and Sb are nearly equal, due to the alloy-scattering of phonons.

Closely related to understanding the bipolar-limited peak *zT* is the contrasted transport properties of the valence and conduction bands. For example, if the conduction band has a significantly higher weighted mobility than the valence band, the n-type material would have less contribution from minority carriers than for the p-type material (for a given E_F). Therefore, quantifying the weighted mobility of the n- and p-type bands is an essential prerequisite for engineering the band structure with an optimum content of Mg_3Bi_2. The contrasted transport properties of n- and p-type have been understood so far only in a rather qualitative matter.

In this study, by modeling both n- and p-type, and also both Mg_3Bi_2-alloyed and non-alloyed Mg_3Sb_2 samples, we illustrate how the DFT-predicted band structure is consistent with the trend of changes in Seebeck effective masses and mobilities seen in transport properties. We then explain how the optimum Mg_3Bi_2 content balances the benefits from increased weighted mobility and reduced lattice thermal conductivity with the disadvantage of a decreased band gap, which enables us to show the origin of the highest peak *zT* composition in $Mg_{3+x}(Sb,Bi)_{2-y}Te_y$.

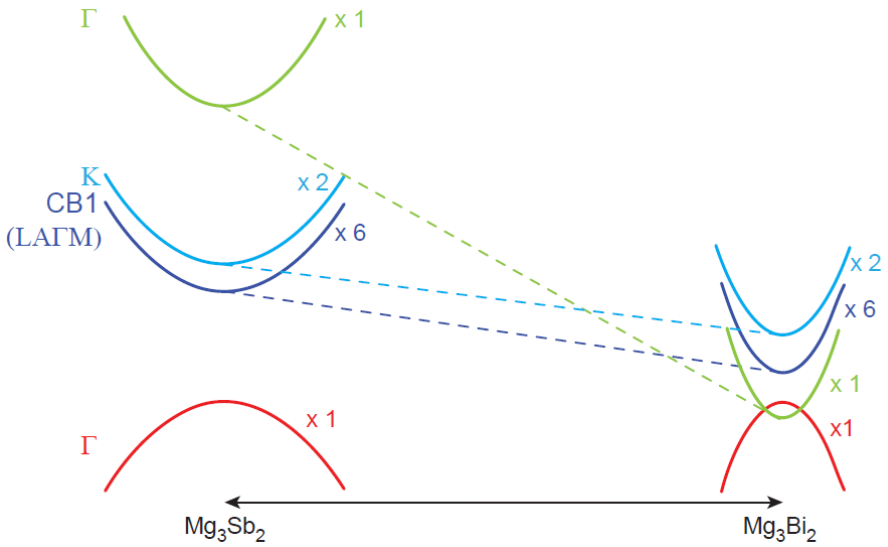

Figure 1 Schematic of changes in the Mg_3Sb_2 band structure due to Mg_3Bi_2 alloying. Alloying leads to a smaller band gap, and also a reduced band effective mass which leads to a higher mobility. The valence band in Mg_3Sb_2 is a single-valley, whereas the conduction band (CB1) is a multi-valley with a degeneracy of six. The minimum of the CB1 band is in the **LAΓM** plane, but not at a high symmetry point; when CB1 is plotted along the **M-L** direction, it apparently appears to have a higher minimum energy than the **K** band.[15,23] The true minimum of the CB1 is significantly lower in energy than the **K** band.[14] The dashed lines illustrate how the Vegard's law would predict the bands to shift (with respect to the valence band). The solid-solution behavior of the material is evidenced from diffraction (see ESI).

Band structure analyzed with m^*_{Seeb} and μ_0

A useful metric that relates the band structure to experimental measurements is the Seebeck effective mass m^*_{Seeb} which is extracted by combining thermopower and Hall measurements (Pisarenko plots).[26] By comparing m^*_{Seeb} and the mobility parameter μ_0 between n- and p-type, or Mg_3Bi_2-alloyed and non-alloyed Mg_3Sb_2 samples, it is possible to infer differences in the band structure. For example, if m^*_{Seeb} is found larger in the n- than p-type, it would indicate a higher density-of-states in the conduction band. Largely, two distinct cases could lead to such a higher density-of-states: presence of either a heavier band (*i.e.* a small curvature at the band edge, heavy m_b^*) or multiple bands (*e.g.* band-degeneracy). In the case of a heavier band, μ_0 would typically be found smaller (assuming that other properties such as the deformation potentials[27] are similar). On the other hand, when multi-valley bands are contributing, μ_0 is identical to that of just a single valley (in the limit of negligible intervalley scattering). If μ_0 is found similar in both n- and p-type despite a large difference in m^*_{Seeb}, then the difference in density-of-states could be attributed to the presence of multiple bands. Therefore, with μ_0 and m^*_{Seeb} pairs, we can see if the transport properties are consistent with the DFT-predicted band structure.

To obtain m^*_{Seeb}, the reduced Fermi-level $\eta = {E_F}/{k_B T}$ is first found from the experimental thermopower by solving the following equation (assumes relaxation time $\tau \propto E^{-1/2}$)[28]:

$$|S(\eta)| = \frac{k_B}{e}\left[\frac{2F_1(\eta)}{F_0(\eta)} - \eta\right] \quad (1)$$

where $F_i(\eta)$ is the Fermi-Dirac integral:

$$F_i(\eta) = \int_0^\infty \frac{\epsilon^i d\epsilon}{e^{\epsilon-\eta}+1} \quad (2)$$

The η determined this way with experimentally measured thermopower could be referred to as an effective value η_{eff} in the sense that we do not necessarily assume the band to be a single parabolic band (Eq1 is often derived with such an assumption[28]). Then the Seebeck effective mass is determined from:

$$m^*_{\text{Seeb}} = \frac{h^2}{2k_B T}\left(n_H \frac{3F_{-0.5}(\eta_{\text{eff}})}{16\pi F_0^2(\eta_{\text{eff}})}\right)^{\frac{2}{3}} \quad (3)$$

Here, n_H is the measured Hall carrier concentration. It is seen from Eq.3 that, for a given η_{eff}, m^*_{Seeb} increases with carrier concentration ($\propto n_H^{2/3}$) indicating that m^*_{Seeb} is related to the density-of-states. We use this procedure on a multiple of samples with different doping levels (*i.e.* different Te content). For samples with the identical type of carriers (n- or p-type) and Mg_3Bi_2 content, m^*_{Seeb} appears to be nearly constant (Fig.2a), indicating that m^*_{Seeb} is a stable way to characterize the conduction and valence bands.

The mobility parameter μ_0 can be extracted from weighted mobility μ_w, which is an essential parameter for thermoelectrics that determines the magnitude of conductivity for a given reduced Fermi-level:

$$\sigma = \frac{e(2m_e k_B T)^{3/2}}{3\pi^2\hbar^3}\mu_w \cdot F_0(\eta) \quad (4)$$

Here m_e is the mass of an electron. The weighted mobility μ_w, is determined by using $\eta = \eta_{\text{eff}}$ in Eq.4 (Fig.2c). Then, μ_0 follows (Fig.2d) from:

$$\mu_w = \mu_0\left(\frac{m^*_{\text{Seeb}}}{m_e^*}\right)^{\frac{3}{2}} \quad (5)$$

using m^*_{Seeb} determined previously (Fig.2a-b). μ_0 is the mobility of a carrier at k_BT higher than the band edge.

It is seen that n-type Mg_3Sb_2 has a larger m^*_{Seeb} than p-type samples (Fig.2b), while μ_0 is similar (Fig.2d). This is a signature consistent with the multi-valley conduction band and single valley valence band structure (Fig.1). It is this multi-valley feature of the conduction band that is mostly responsible for the superior μ_w, and thus the better thermoelectric performance of the n-type. The ratio of the m^*_{Seeb} between n- and p-type is about 1.9, somewhat smaller than $(N_V=6)^{2/3}$ =3.3 which indicates that the m_b^* of the individual conduction pocket could be lighter than the valence band pocket rather than being similar.

The Mg_3Bi_2 alloying effect is seen by the monotonic decrease in m^*_{Seeb} with increasing Mg_3Bi_2 content (Fig.2b), accompanied with an increase in μ_0 (Fig.2d). This trend is seen in both n- and p-type samples, and suggests the band masses are becoming lighter with alloying, as opposed to band convergence which should give a peak in m^*_{Seeb}.[12] Lighter band masses typically give better μ_w for carriers scattered by phonons, as is indeed observed in Fig.2c. An increased μ_w is always beneficial for thermoelectrics (other than that it usually accompanies a reduced band gap), as we can see from the definition of the dimensionless material quality factor *B:* [26,29–31]

$$B = \left(\frac{k_B}{e}\right)^2 \frac{e(2m_e k_B T)^{3/2}}{3\pi^2\hbar^3}\frac{\mu_w}{\kappa_L}T \quad (6)$$

where κ_L is lattice thermal conductivity. *B* determines the maximum *zT* obtainable at a given temperature when the carrier concentration is optimized. For example, *B* of n-type Mg_3Sb_2 at 600 K is increases from 0.2-0.25 to 0.5-0.6 after alloying with 25% of Mg_3Bi_2, predicting an increase in the maximum *zT* from 0.6 to 1.3 at 600 K. Half of the increase in *B* is attributed to the increase in μ_w.

Therefore, Mg_3Bi_2-alloying is seen to lead to better performance not just because of the lattice thermal conductivity reduction discussed in the literature, but also because of the significantly improved electronic properties.

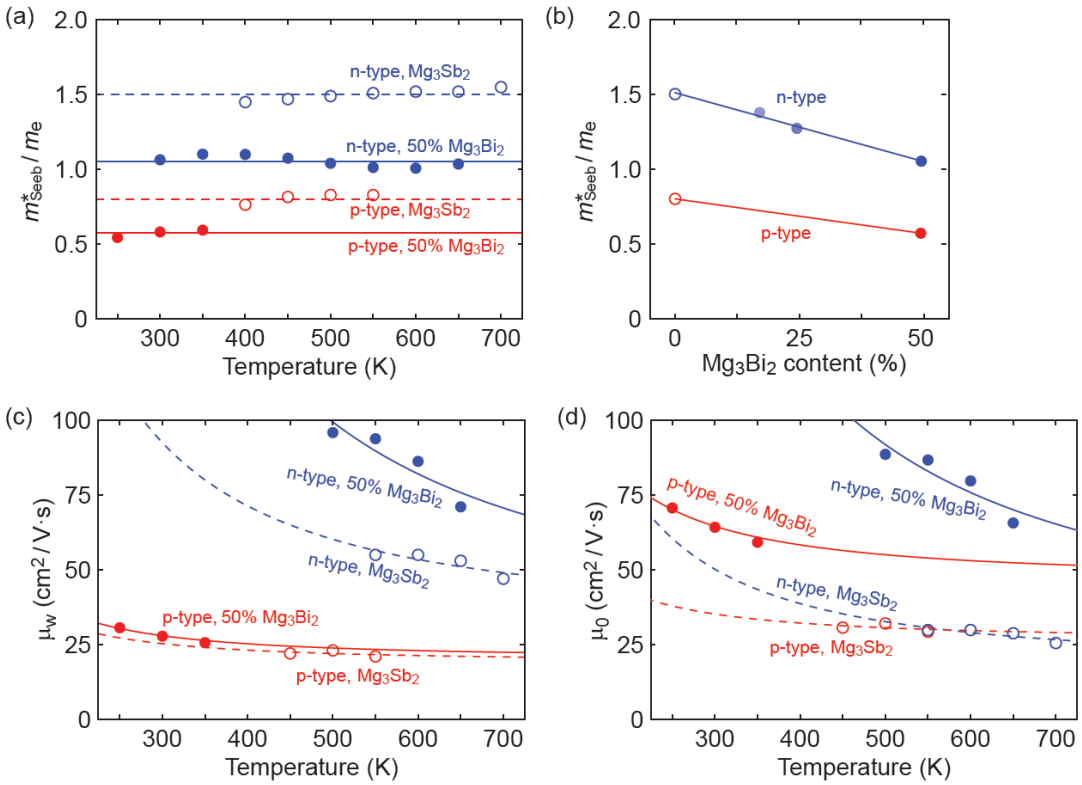

Figure 2 (a,b) Seebeck effective mass of the Mg_3Sb_2 (open circles) and Mg_3Sb_2-Mg_3Bi_2 alloy (filled circles) samples. **(c)** Weighted mobility and **(d)** Mobility parameter as a function of temperature. The lines show a fit to the $\mu_w \propto T^{-3/2}$ dependency (phonon scattering). All data points are from temperatures where bipolar conduction is not significant, representing the property of majority carriers. For weighted mobility, the low-temperature points where the mobility is grain-boundary limited[32,33] was excluded. The p-type Mg_3SbBi data were taken from Ref.[[18]]. All other data are from the current study.

Band gap and bipolar effects analyzed with the peak thermopower

Alloying with Mg_3Bi_2 is expected to reduce the band gap, as can be seen in Fig.1. The alloying effect on the band gap can be analyzed by the Goldsmid-Sharp gap, together with a correction method. The Goldsmid-Sharp gap E_{GS} is found from the peak thermopower (S_{max}) with respect to temperature and the temperature at which it occurs (T_{max}).

$$E_{GS} = 2e|S_{max}|T_{max} \quad (7)$$

This relation is associated with the fact that thermopower stops increasing with temperature due to the onset of minority carrier conduction in heavily doped semiconductors. E_{GS} is, however, not the true gap E_g but an effective gap because minority carrier conduction also depends on their weighted mobility. For example, if the minority carriers have low μ_w relative to the majority carriers, the bipolar effect is suppressed, leading to higher S_{max} and E_{GS} for a given true band gap (therefore, E_{GS} being higher than E_G is a desirable characteristic of a thermoelectric material). It has been demonstrated previously how to determine the true gap by correcting E_{GS} using the weighted mobility ratio between the majority and minority carriers.[34]

Using the μ_w and E_{GS} extracted for both n- and p-type samples with different Mg_3Bi_2 content, we find the true gap 0.54 eV (±0.05 eV due to uncertainty in T_{max}) for Mg_3Sb_2 and its linear decrease with increasing Mg_3Bi_2 content in the $Mg_{3+x}Sb_{2-y}Bi_y$ solid solution (Fig.3a). As expected from the contrast in weighted mobilities, the uncorrected band gap E_{GS} (open circle in Fig.3a) of n- is much higher than that of the p-type. By using the correction method,[34] consistent estimates of the true band gap E_g were obtained. The decreasing trend in the band gap with respect to Mg_3Bi_2 content extrapolates to a negative gap at pure Mg_3Bi_2, which is indeed reported to show semi-metallic behavior.[18–20,22,23]

The advantage of the high contrast in n- and p-type μ_w's is readily noticeable in the comparison of n- and p-type thermopower curves with respect to temperature (Fig.3b). S_{max} and T_{max} are higher in n-type, which is beneficial in reaching a higher peak *zT*, at the expense of lower values in the p-type.

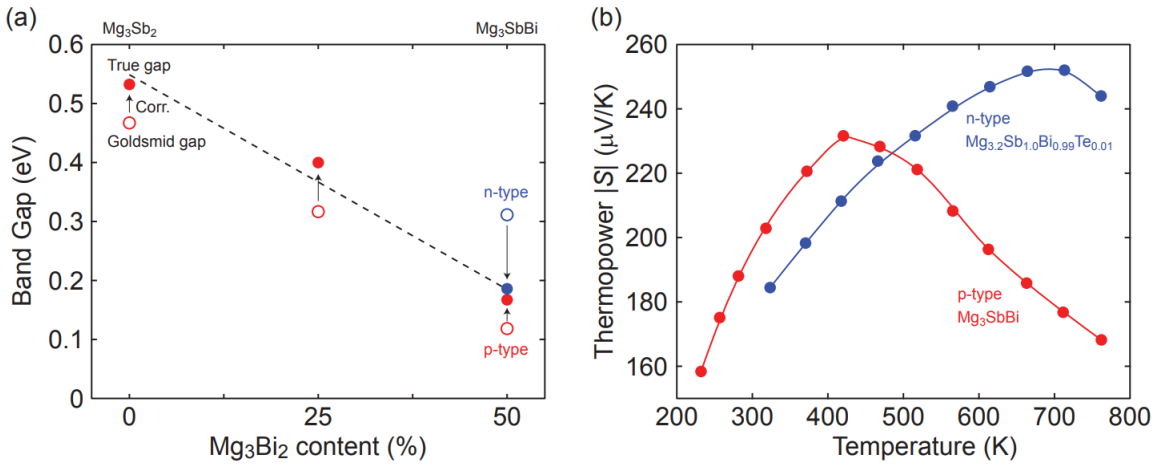

Figure 3 (a) The reduction in band gap due to alloying with Mg_3Bi_2. Open circles represent the Goldsmid gap estimated by Eq.7. The solid circles are estimations of the true gap by using a correction method that uses the μ_w ratio between n- and p-type carriers.[34] The true gaps individually estimated from n- and p-type samples coincide. Linear interpolation of the trend for the true gap is shown in a dashed line. **(b)** Thermopower peaks with respect to temperature shown for n- and p-type Mg_3SbBi (similar Mg_3Bi_2 content). The peak thermopower shows a higher value at a higher temperature in n-type, which indicates a higher μ_w for the n-type carriers.

The optimum Mg_3Bi_2 content for thermoelectrics

Whether a larger band gap, which leads to a higher peak *zT* at a higher temperature, could be useful depends on the stable temperature range of the material. The maximum operation temperature must be decided to gauge the benefits of widening the band gap.

Experimentally it has been noticed that Mg_3Sb_2 is not stable over long periods above 750 K due to the high vapor pressure of Mg, which leads to a decrease in the solubility of the n-type dopants (*i.e.* Te) and thus a loss of n-type carriers.[16] Therefore, for deciding the optimum Mg_3Bi_2 content, we assume the maximum operation temperature for Mg_3Bi_2-alloyed samples to be around 700-750 K, and limit the optimization space to where the peak *zT* is found below this temperature.

We note that the expected peak *zT* temperature is above the maximum operation temperature in

Mg_3Sb_2. As shown in Fig.4, the *zT* values of Mg_3Sb_2 samples are still increasing after the maximum operation temperature. A higher *zT* value would be achievable if the sample were to reach a higher temperature (which is not possible due to stability). Because the peak *zT* is stability-limited rather than band-gap limited in Mg_3Sb_2, it is beneficial to reduce the band gap until the peak *zT* temperature is within the stability range and gain an increased μ_w. Because of this stability limit, we found that alloying Mg_3Bi_2 up to 25% is purely beneficial without compromises in any transport properties. Alloying Mg_3Bi_2 much more than this amount results in a lower *zT* peak value at a lower temperature as shown by the case of $Mg_{3+x}Sb_{1.00}Bi_{0.99}Te_{0.01}$.

The optimum Mg_3Bi_2 content is found by collectively considering the impact of Mg_3Bi_2 alloying on the band-gap, μ_w and also lattice thermal conductivity. We linearly interpolate μ_w and E_g with respect to Mg_3Bi_2 content as an empirical estimation. For lattice thermal conductivity, we describe the approximate trend by using the relation between $\kappa_{L,alloy}$ and $\kappa_{L,pure}$ proposed by Callaway[35] and Klemens.[36]

$$\frac{\kappa_{L,alloy}}{\kappa_{L,pure}} = \frac{\arctan(u)}{u}$$

$$u^2 = \frac{\pi\theta_D\Omega}{2\hbar v^2}\kappa_{L,pure}\Gamma$$

Here θ_D is the Debye temperature, Ω is the volume per atom, v is the average speed of sound, and Γ is the scattering parameter mainly caused by mass fluctuation. Γ can be calculated by the modified Klemens model.[5] Then, by combining these data, we calculate the peak *zT* below 725 K as a function of Mg_3Bi_2 content (Fig.5). We find the optimum Mg_3Bi_2 composition in the range of 20-30 % which is indeed close to the experimentally successful composition reported in the literature.[14]

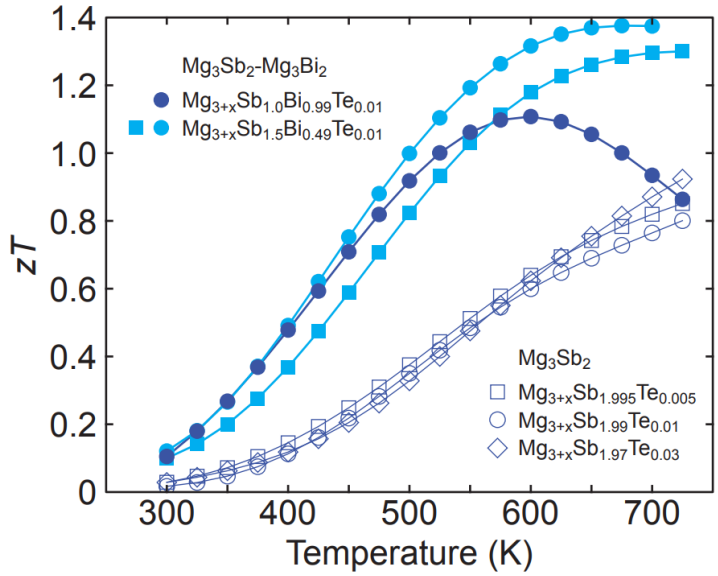

Figure 4 *zT* curves of Mg_3Sb_2 and Mg_3Sb_2-Mg_3Bi_2 alloy n-type samples. Around the thermal stability limit (700-750 K), the *zT* of Mg_3Sb_2 samples show an increasing trend. With the addition of Mg_3Bi_2, the peak is shifted to lower temperatures near or below the stability limit.

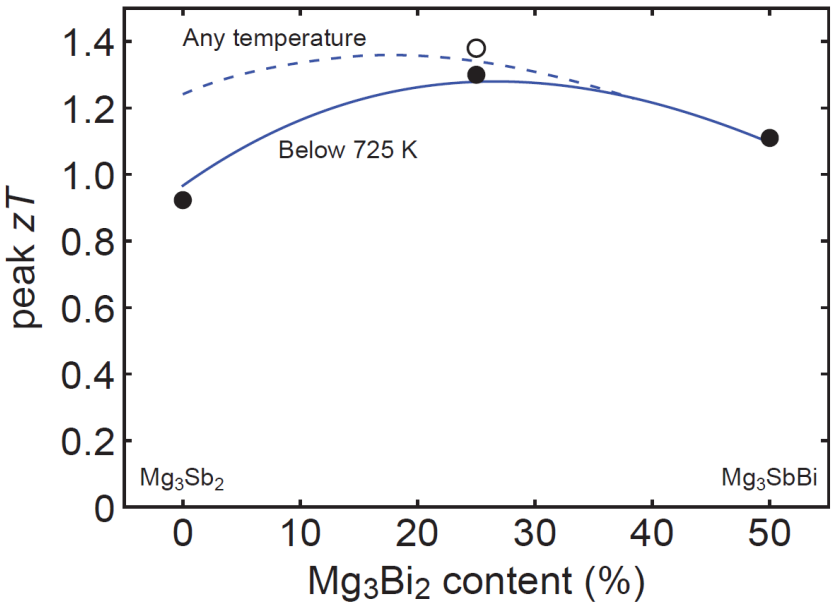

Figure 5 Peak *zT* as a function of the Mg_3Bi_2 alloyed with Mg_3Sb_2. Model calculation for the peak *zT* below 725 K (stability temperature) is indicated with the solid line, while the peak *zT* within an unrestricted temperature limit is shown with the dashed line. It is seen that the peak *zT* is stability-temperature-limited up to 30-40 % of Mg_3Bi_2 content. The optimum is found in the range of 20-30 % Mg_3Bi_2 content. Experimental values are plotted together for comparison (circles). The open circle corresponds to a sample with lower than typical lattice thermal conductivity and thus a higher *zT*.[37]

Conclusion

The electronic structure of Mg_3Sb_2 and its alloy with Mg_3Bi_2 was studied by analyzing the transport properties with an effective mass approach. Heavier Seebeck effective mass and larger weighted mobility in n- than p-type were observed, which is a signature of the higher band degeneracy of the conduction band. Mg_3Sb_2-Mg_3Bi_2 alloys showed a decrease in Seebeck effective mass and increase in weighted mobility, indicative of a larger curvature in each individual band (lighter band mass). This change accompanied a decrease in the band gap. Since the band gap of the Mg_3Sb_2 (0.5-0.6 eV) makes the *zT* peak at a temperature higher than the stability limit, we find the Mg_3Bi_2-alloying to be electronically beneficial for thermoelectrics despite the reduction in band gap. By empirically modeling the transport property changes due to alloying, we find the optimum Mg_3Bi_2 content in the range of 20-30 %, which is in good agreement with the experimental observation.

Experimental method

Pure elemental materials of magnesium turnings (99.98 %, Alfa Aesar), antimony shots (99.9999 %, Alfa Aesar), bismuth granules (99.997 %, Alfa Aesar) and tellurium lumps (99.999 %, Alfa Aesar) were loaded according to the nominal composition and sealed into stainless-steel vials with two half inch stainless-steel balls inside the argon-filled glove box. Mechanical reaction was conducted by high energy-ball milling with a high-energy mill (SPEX 8000D) for two hours. The reacted powder was extracted from vials and transferred into a graphite die under argon atmosphere to prevent the oxidization of the materials. Subsequently, induction heating rapid hot press was conducted for 1 hour at 873 K and 45 MPa under argon gas flow to consolidate pellet samples.[38] Pressed samples were gradually cooled down to room temperature with no load. The Seebeck coefficient of each sample was measured with Chromel-Nb thermocouples in a two-probe configuration under high vacuum.[39] The Hall coefficient and electric resistivity was measured simultaneously using a 4-point probe Van der

Pauw technique with a 2 T magnetic field under high vacuum. Thermal diffusivity D was measured by using the flash method with a Netzsch LFA 457 under dynamic argon atmosphere. The thermal conductivity κ was calculated by $\kappa = D \times C_p \times d$, where d is the geometrical density and C_p is the heat capacity. Average values of the heat capacity reported in previous studies (Tamaki et al.[14] for Mg_3Bi_2-alloyed samples, Bhardwaj et al.[40] for non-alloyed Mg_3Sb_2 samples) were used for the calculations.

Acknowledgements
The authors would like to acknowledge support from the U.S. Department of Energy, Office of Science, Basic Energy Sciences through the Solid-State Solar-Thermal Energy Conversion Center (S3TEC), an Energy Frontier Research Center (DE-SC0001299), and also from the NASA Science Mission Directorate's Radioisotope Power Systems Thermoelectric Technology Development program. KI acknowledges support from Funai Foundation for Information Technology.

References

1 L. E. Bell, *Science*, 2008, **321**, 1457–1461.
2 G. J. Snyder and E. S. Toberer, *Nat. Mater.*, 2008, **7**, 105–114.
3 A. Zevalkink, J. Swallow, S. Ohno, U. Aydemir, S. Bux and G. J. Snyder, *Dalton Trans.*, 2014, **43**, 15872–15878.
4 H. Wang, A. D. Lalonde, Y. Pei and G. J. Snyder, *Adv. Funct. Mater.*, 2013, **23**, 1586–1596.
5 J. Yang, G. P. Meisner and L. Chen, *Appl. Phys. Lett.*, 2004, **85**, 1140–1142.
6 Y. Pei and D. T. Morelli, *Appl. Phys. Lett.*, 2009, **94**, 122112.
7 E. S. Toberer, A. F. May, B. C. Melot, E. Flage-Larsen and G. J. Snyder, *Dalt. Trans.*, 2010, **39**, 1046–1054.
8 F. Gascoin, S. Ottensmann, D. Stark, S. M. Haïle and G. J. Snyder, *Adv. Funct. Mater.*, 2005, **15**, 1860–1864.
9 H. Wang, Z. M. Gibbs, Y. Takagiwa and G. J. Snyder, *Energy Environ. Sci.*, 2014, **7**, 804–811.
10 W. Liu, X. Tan, K. Yin, H. Liu, X. Tang, J. Shi, Q. Zhang and C. Uher, *Phys. Rev. Lett.*, 2012, **108**, 166601.
11 Y. Pei, X. Shi, A. LaLonde, H. Wang, L. Chen and G. J. Snyder, *Nature*, 2011, **473**, 66–69.
12 H. S. Kim, N. A. Heinz, Z. M. Gibbs, Y. Tang, S. D. Kang and G. J. Snyder, *Mater. Today*, 2017, **20**, 452–459.
13 Y. Tang, Z. M. Gibbs, L. a Agapito, G. Li, H.-S. Kim, M. B. Nardelli, S. Curtarolo and G. J. Snyder, *Nat. Mater.*, 2015, **14**, 6–12.
14 H. Tamaki, H. K. Sato and T. Kanno, *Adv. Mater.*, 2016, **28**, 10182–10187.
15 J. Zhang, L. Song, S. H. Pedersen, H. Yin, L. T. Hung and B. B. Iversen, *Nat. Commun.*, 2017, **8**, 13901.
16 S. Ohno, K. Imasato, S. Anand, H. Tamaki, S. D. Kang, P. Gorai, H. K. Sato, E. S. Toberer, T. Kanno and G. J. Snyder, *Joule*, accepted.
17 J. Shuai, J. Mao, S. Song, Q. Zhu, J. Sun, Y. Wang, R. He, J. Zhou, G. Chen, D. J. Singh, Z. Ren, C. W. Chu, G. Chen and Z. Ren, *Energy Environ. Sci.*, 2017, **10**, 799–807.
18 V. Ponnambalam and D. T. Morelli, *J. Electron. Mater.*, 2013, **42**, 1307–1312.
19 H. X. Xin and X. Y. Qin, *J. Phys. D Appl. Phys.*, 2006, **39**, 5331–5337.
20 S. H. Kim, C. M. Kim, Y.-K. Hong, K. I. Sim, J. H. Kim, T. Onimaru, T. Takabatake and M.-H. Jung, *Mater. Res. Express*, 2015, **2**, 55903.
21 C. L. Condron, S. M. Kauzlarich, F. Gascoin and G. J. Snyder, *J. Solid State Chem.*, 2006, **179**, 2252–2257.
22 R. P. Ferrier and D. J. Herrell, *J. Non. Cryst. Solids*, 1970, **2**, 278–283.
23 Y. Imai and A. Watanabe, *J. Mater. Sci.*, 2006, **41**, 2435–2441.
24 W. G. Zeier, A. Zevalkink, Z. M. Gibbs, G. Hautier, M. G. Kanatzidis and G. J. Snyder, *Angew. Chemie Int. Ed.*, 2016, **55**, 6826–6841.
25 S. D. Kang, P. Jan-hendrik, U. Aydemir, P. Qiu, C. C. Stoumpos, R. Hanus, M. Anne, X. Shi, L. Chen, M. G. Kanatzidis and G. J. Snyder, *Mater. Today Phys.*, 2017, **1**, 7–13.
26 S. D. Kang and G. J. Snyder, 2017, ArXiv 2017, arXiv:1710.06896 [cond-mat.mtrl-sci],

https://arxiv.org/abs/1710.06896.
27 J. Bardeen and W. Shockley, *Phys. Rev.*, 1950, **80**, 72–80.
28 A. F. May and G. J. Snyder, in *Materials, Preparation, and Characterization in Thermoelectrics*, ed. D. M. Rowe, CRC Press, 2012, pp. 1–18.
29 R. P. Chasmar and R. Stratton, *J. Electron. Control*, 1959, **7**, 52–72.
30 S. D. Kang and G. J. Snyder, *Nat. Mater.*, 2016, **16**, 252–257.
31 S. Ohno, A. Zevalkink, Y. Takagiwa, S. K. Bux and G. J. Snyder, *J. Mater. Chem. A*, 2014, **2**, 7478–7483.
32 J. Kuo, S. D. Kang and G. J. Snyder, *unpublished*.
33 T. Kanno, H. Tamaki, S. Hiroki, S. D. Kang, S. Ohno, K. Imasato, J. Kuo, G. J. Snyder and Y. Miyazaki, *unpublished*.
34 Z. M. Gibbs, H.-S. Kim, H. Wang and G. J. Snyder, *Appl. Phys. Lett.*, 2015, **106**, 22112.
35 J. Callaway and H. von Baeyer, *Phys. Rev.*, 1960, **120**, 1149–1154.
36 P. Klemens, *Phys. Rev.*, 1960, **119**, 507–509.
37 K. Imasato, S. Ohno, S. D. Kang and G. J. Snyder, *unpublished*.
38 A. D. LaLonde, T. Ikeda and G. J. Snyder, *Rev. Sci. Instrum.*, 2011, **82**, 25104.
39 S. Iwanaga, E. S. Toberer, A. Lalonde and G. J. Snyder, *Rev. Sci. Instrum.*, 2011, **82**, 63905.
40 A. Bhardwaj and D. K. Misra, *RSC Adv.*, 2014, **4**, 34552–34560.